Carbon 239 (2025) 120301

Contents lists available at ScienceDirect

Carbon

journal homepage: www.elsevier.com/locate/carbon

Self-detached laser induced graphene derived from bio-oil distillation residues for multifunctional applications

Shuhong Yang [a], Yaseen Elkasabi [b], Qiangu Yan [c], Bujingda Zheng [d], Honghua Qian [d], Jian Lin [d], Caixia Wan [a,*]

[a] Department of Chemical and Biomedical Engineering, University of Missouri, 1406 East Rollins Street, Columbia, MO, 65211, USA
[b] Eastern Regional Research Center, USDA Agricultural Research Service, U.S. Department of Agriculture, 600 East Mermaid Lane, Wyndmoor, PA, 19038, USA
[c] Forest Products Laboratory, USDA Forest Service, One Gifford Pinchot Drive, Madison, WI, 53726, USA
[d] Department of Mechanical and Aerospace Engineering, University of Missouri, 416 South 6th Street, Columbia, MO, 65211, USA

ARTICLE INFO

Keywords:
Bio-oil distillation residues
Laser induced graphene
Direct laser writing
Supercapacitors
Electronics

ABSTRACT

This study reported laser induced graphene (LIG) fabricated from the distillation residues of bio-oil resulting from switchgrass pyrolysis. The bio-oil distillation residues as a precursor can significantly boost the efficiency of LIG synthesis by generating self-detachable and standalone LIG layers via direct laser writing toward high-throughput roll-to-roll manufacturing. For on-chip applications, the produced LIG had high specific surface area (375.30 m^2/g) and excellent electrical conductivity, which can be facilely transferred onto adhesive substrates with fully preserved structural integrity by direct dry peel-off. The LIG-based sensor exhibited remarkable sensitivity to strains (e.g., bending, vibration), temperature, and humidity. Even when subjected to 250 Hz vibrations with ~0.2 mm amplitude, the sensor accurately captured the periodical signal change at a 25 Hz signal collecting rate. The supercapacitors also exhibited the high energy density (E_A) of 27.3 μW h/cm^2 with the power density (P_A) of 0.089 mW/cm^2 and the specific area capacitance (C_A) of 248.7 mF/cm^2 at the current density of 0.2 mA/cm^2. These findings suggest the tremendous potential of biomass derived LIG in large-scale manufacturing for energy storage devices, environment monitoring sensors, and wearable electronics.

1. Introduction

Laser induced graphene (LIG) has emerged as a versatile advanced carbon material for thin-film and 3D electrodes [1–6]. Various low-cost, eco-friendly biomass-derived LIG has been explored as electrodes for flexible and wearable electronic devices for energy storage and sensing [7,8]. Those applications can be categorized into two main groups: (1) on-chip applications developed on original biomass-based substrates, such as electronics assembled on *in situ* LIG-embedded wood [9–11]; and (2) applications fabricated with transferred LIG, such as LIG-silicone composites for wearable devices [8,12,13]. While on-chip application based on *in situ* embedded LIG entails strong adherence of LIG on its original substrates, LIG transfer to another substrate is the opposite demanding easy detachment. Facile techniques for LIG transfer usually involve infiltrating and curing an elastomer liquid (usually PDMS) on LIG surface followed by peeling off LIG-embedded composite with manually applied vertical pressure and horizontal peeling force [14–16]. For some biomass-based substrates, such as paper and lignin films, a technique, so-called water lift, has also been adopted to detach LIG by dissolving uncarbonized substrates in water [12,17]. However, those transfer methods do not consider immediate reusability of the precursor, which is indeed crucial for large-scale LIG production [17]. Another limitation is LIG loss and damage during its transfer processes, leading to poorly preserved structural integrity of transferred LIG and performance of derived electronics [18]. Therefore, from the perspective of LIG transfer, easy detachment for LIG from its original substrate would ensure structural integrity and functions of derived electronics [6]. To our best knowledge, no substrates have yet to be developed for self-detached, free-standing LIG featuring effortless transfer while being reusable toward continuous laser writing for quality LIG products.

Bio-oil distillation involves depolymerization and dehydration that converts complex organic polymers into simpler molecules while generating solid residues alongside heavier liquid fractions for further refining [19]. With advancements in bio-oil production via fast pyrolysis and its refining, large quantities of bio-oil distillation residues (BDRs) are generated as byproducts. Those residues exhibit a highly aromatic

* Corresponding author.
E-mail address: wanca@missouri.edu (C. Wan).

https://doi.org/10.1016/j.carbon.2025.120301
Received 14 November 2024; Received in revised form 28 March 2025; Accepted 5 April 2025
Available online 7 April 2025
0008-6223/© 2025 Elsevier Ltd. All rights reserved, including those for text and data mining, AI training, and similar technologies.

nature, enhanced chemical homogeneity, and reduced oxygen content and functional groups [20]. The key to generating high-quality LIG during DLW is effective conversion of sp^3 carbon bonds in a precursor into sp^2 hybridized structures through intense photon energy [21,22]. Aromatic structures with homogeneous and carbon-enriched compositions are particularly advantageous for rearranging into a honeycomb-like graphene network [23–25]. Considering intrinsic characteristics, BDRs would have great potential to be a precursor for high-quality LIG production. The integration of bio-oil distillation with LIG synthesis would present a novel and sustainable pathway for advancing both thermochemical biorefinery and advanced carbon industries.

The main objective of this work was to explore BDRs as a novel precursor for LIG synthesis and subsequent applications in supercapacitors (SCs) and sensors. It would address the need for sustainable and cost-effective development of wearable electronics using transferred LIG. The BDR-based substrates were well developed via solvent optimization to enable self-detachment of intact LIG while sustaining repeated scribing cycles. The reusability of the substrate and the quality consistency of LIG from multiple laser scribing cycles were also evaluated. The peeled-off LIG was incorporated into flexible electronics, i.e., high-performance SCs, and ultrasensitive temperature and humidity sensors. Overall, this work demonstrated BDRs as a novel biomass-derived precursor for high-throughput LIG synthesis and high-performance LIG-based electronics.

2. Material and methods

2.1. Materials

BDRs were collected from bio-oil distillation process that was conducted in the USDA-ARS Eastern Regional Research Center (Wyndmoor, Pennsylvania, USA). The detailed procedure for generating BDRs is described in the Supporting Information. All the other chemicals were purchased from Fisher Scientific (Hampton, New Hampshire, USA) and used as received.

2.2. LIG synthesis

The precursor (BDRs) solution was prepared as detailed in the Supporting Information and then mixed with 10 g of 9 wt% polyvinyl alcohol (PVA, M_W 146,000–186,000) solution until a dark brown liquid was obtained. The liquid was poured in a plastic Petri dish (9 cm in diameter) and dried at 35 °C in an environmental chamber (25–50 % humidity) until a constant weight was obtained. After drying, the lignin film was removed from the Petri dish and affixed to a glass slide for laser writing.

A CO_2 laser machine (30W, VLS3.50, Universal Laser Systems Inc, Scottsdale, Arizona, USA) was used for DLW. All laser scribing tests were conducted under ambient conditions. Laser power with different levels (i.e., 20 %, 40 % and 60 % of the upper limit of laser power setting) were tested, while 10 % speed, 1000 pulses per inch, and 2-mm defocus were consistently applied. LIG samples were labeled as LIG-x, where x stands for the number of cycles of laser scribing at the same area on a BDR substrate.

2.3. Fabrication of SCs and sensors

LIG patterned on the film was directly taped off by lab labeling tape (Queens, New York, USA). Copper tape was then attached at the ends of transferred LIG electrodes using conductive silver paste (Ted Pella Inc, Redding, California, USA) followed by air drying for 20 min. The assembly was directly used as sensors or further applied with KOH/PVA gel electrolyte (detailed in the Supporting Information) for SC fabrication. In brief, Kapton tape was used to cover the ends of two electrodes followed by applying KOH/PVA gel electrolyte. After air drying for 12 h, Kapton tape was applied on the top, obtaining the complete assembly of SCs.

2.4. LIG characterization

Raman spectra of LIG were acquired on an inVia™ confocal Raman microscope (Renishaw, West Dundee, Illinois, USA) with a wavelength of 633 nm. Scanning electron microscope (SEM) equipped with a Bruker Quantax 200 Silicon Drift Detector (FEI Quanta 600 FEG, FEI company, Hillsboro, Oregon, USA) was used for SEM imaging, operated at 5 or 20 kV and 100 pA. High-resolution transmission electron microscopy (HRTEM) images were acquired on a ThermoScientific Spectra 300 microscope (Biotechnology company, Berkeley, Missouri, USA) operated at 300 kV. The LIG powder scraped off from the scribed film was sonicated in ethanol for 10 min before HRTEM imaging. Sheet resistance (Rs) was measured using a Pro-4 Four Point Resistivity Systems (Lucas Labs, Gilroy, California, USA). Brunauer-Emmett-Teller specific surface area (S_{BET}) analysis for BDR-derived LIG was measured with a TriStar II 3020 3.02 (Micromeritics, Norcross, Georgia, USA).

2.5. Evaluation of electrochemical performance of SCs

Cyclic voltammetry (CV), galvanostatic charge-discharge (GCD), and electrochemical impedance spectroscopy (EIS) measurements were performed on an electrochemical station (Metrohm Autolab, B.V-GSTST128 N, Herisau, Switzerland) using a 2-electrode testing mode.

Areal capacitance (C_A) (mF/cm^2) was calculated using the GCD test data following Equation (1) below:

$$C_A = \frac{I}{S \times \left({dV}/{dt} \right)} \tag{1}$$

where I is the applied charge-discharge current (mA), S is the active surface area of the electrode (0.7 cm^2, as depicted in Fig. S1), and dV/dt is the slope of the galvanostatic discharge curve.

E_A ($\mu Wh/cm^2$) was subsequently calculated following Equation (2):

$$E_A = \frac{1}{2} \times C_A \times \frac{(\Delta V)^2}{3600} \times 1000 \tag{2}$$

where ΔV is the potential difference (V).

Power density P_A (mW/cm^2) was calculated using Equation (3):

$$P_A = \frac{E_A}{1000\ \Delta t} \times 3600 \tag{3}$$

where E_A was calculated following Equation (2), and Δt is the discharge time (s).

2.6. Electrical measurements for sensors

Resistance signal changes of LIG electrodes used for sensing were continuously monitored by an LCR meter (Keithley 6514, Cleveland, Ohio, USA) operated at a direct current voltage of 1 V. For bending sensing, the sensor was evaluated when placed at different angles (0°, 45°, 90°, 135°, and 180°), controlled by two glass plates with one side closely attached to each other. To detect vibration, a shaker (B&K V203, Bruel & Kjaer, Duluth, Georgia, USA) was used to vibrate the sensor at different frequencies (0, 100, 150, and 250 Hz), with a vibration amplitude of ~0.2 mm. For the temperature sensing testing, the sensor was placed horizontally in a convention oven at different temperatures (35, 39, 43, 47, 51, 54, and 56 °C) for 1 min.

3. Results and discussion

3.1. Highly transferable LIG and reusable substrate

To develop a homogenous LIG precursor, the BDRs were dissolved in the alkaline/MEK solution before film casting (Figs. S2 and S3). Compared to the NaOH solution, the alkaline MEK solution promoted complete dissolution of BDRs (Fig. S4). The BDR film made from the alkaline MEK solution exhibited a smoother surface with more even distribution of carbon atoms (Fig. S4). In addition, the film exhibited excellent reusability and capability to generate self-detached and highly flexible LIG layer (Fig. 1a). A BDR film with 2.15-mm thickness can sustain 5 cycles of laser scribing at the same area for lasing (Video S1), demonstrating the high graphene conversion efficiency of this precursor. Interestingly, after each cycle, the LIG layer auto-detached from the substrate after leaving the scribed substrate under ambient conditions for about 5 min, forming a standalone membrane-like layer (Video S2). This phenomenon could be attributed to the absence of strong chemical bonds, which reduced the adhesion between the LIG and substrate surface [26–28]. Specifically, BRDs are predominantly aromatic and lack noticeable reactive functional groups as a result of bio-oil distillation [20]. Thus, limited interactions between the carbonized/graphitized layer and substrate could promote the facile separation of LIG from the original surface. Furthermore, differences in the thermal and hygroscopic expansion coefficients between the LIG and film substrate can induce internal forces that could also promote LIG detachment [29], which was evidenced by self-detached LIG flakes with certain degrees of curvature (Video S2 and S3). Thus, the technique for fabricating stand-alone LIG in this work featured quick auto-/self-detachment under ambient condition due to the nature of precursor and its film substrate. It was distinct from the prior work that pioneered free-standing LIG via the post-treatment of laser-scribed polybenzoxazine substrates with liquid nitrogen [30]. Further, we demonstrated direct tape peeling as an exemplary transfer technique for low-cost and disposable green electronics (Video S3) as discussed in the latter sections. In short, the reusable BDR film substrate allowed direct peeling/clean detachment of LIG for effortless transfer under ambient condition, offering significant cost-effectiveness and sustainability for high-throughput LIG production. It is worthy to note auto-detached LIG also appeared to be free-standing, which would open new avenues to downstream applications. Such unique standalone feature will be explored in our future study.

The 40 % laser power level resulted in the highest quality of LIG-1 as revealed by Raman Spectra (Fig. S5), which was thus selected as an optimal level for multi lasing cycles. LIG-1, -3, and -5 were characterized and compared for quality consistency. The Raman spectra of all these LIG samples exhibit three distinct peaks (Fig. 1b): D peak (~1360 cm^{-1}, indicating defects and distortions in sp^2 carbon bonds), G peak (~1580 cm^{-1}, arising from the first-order band of sp^2 hybridized carbon bonds), and 2D peak (~2670 cm^{-1}, originating from second-order zone boundary phonons). Consistent I_D/I_G ratio of ~0.8 and sheet resistances of ~40 Ω sq^{-1} were observed with all those LIG samples (Fig. S6). The symmetric level analyses of 2D peaks in their Raman spectra revealed that all R^2 values of the curve fitting were greater than 0.985 (Fig. S7), indicating the synthesized LIG can be well characterized as graphene [31]. The HRTEM image of LIG-3 revealed fringe-like patterns of the graphene layers with *d*-spacing of 0.34 nm between adjacent (002) planes [32,33], showing layer numbers approximately from 5 to 10 (Fig. 1c and d). EDS mapping for LIG-1, -3, and -5 showed that all the samples had similar contents of carbon (C), oxygen (O), and sodium (Na) as the main elements (Fig. 2a–c and S8). The nitrogen (N) content also remained consistent at ~1.4 %. Such a small amount of N originated from the BDR precursor (Table S1). Those results further confirmed the film's reusability for generating LIG with high quality and consistency toward mass production.

Interestingly, abundant microspheres appeared in the LIGs (Fig. 2), which were not observed in most LIG derived from other types of precursor (e.g., paper, wood, PI) [9,34–36]. The SEM images show that those microspheres had diameters ranging from 5 to 10 μm with relatively uniform distribution. Chemical compositions of precursor, film preparation, and laser conditions could all contribute to the microspheres formation [37,38]. To gain a deeper understanding, we explored the factors such as different loadings of the precursor (i.e., 21, 48, and 59 wt%) in the film and types of alkali (NaOH vs. KOH) used for the film

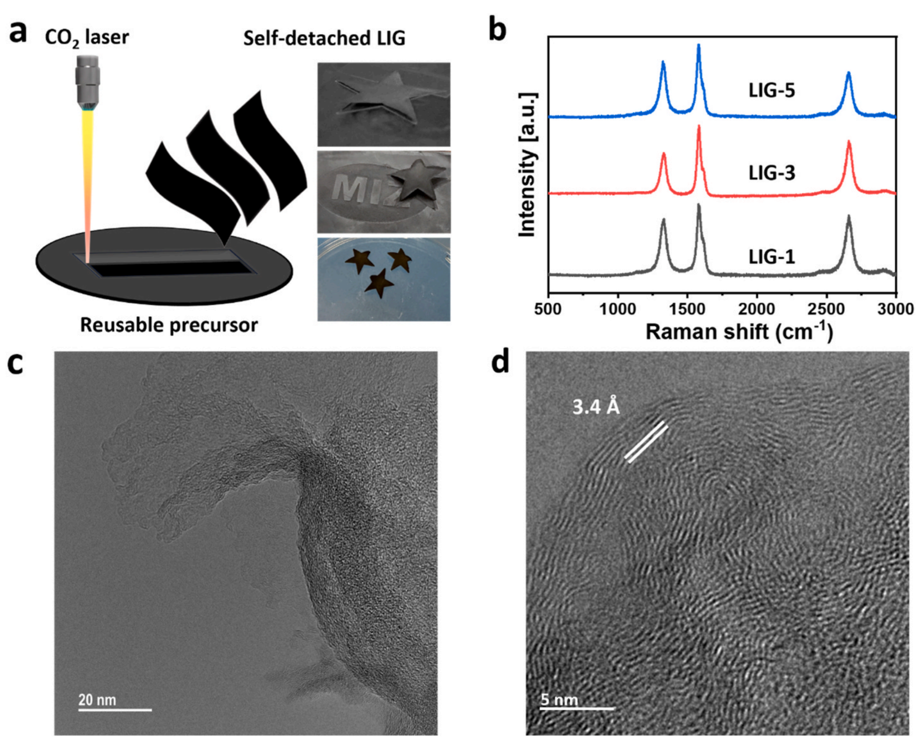

Fig. 1. LIG fabrication and characterization. (a) Schematic diagram of DLW with detached LIG, (b) Raman spectra of LIG samples, and (c–d) HRTEM images of LIG-3.

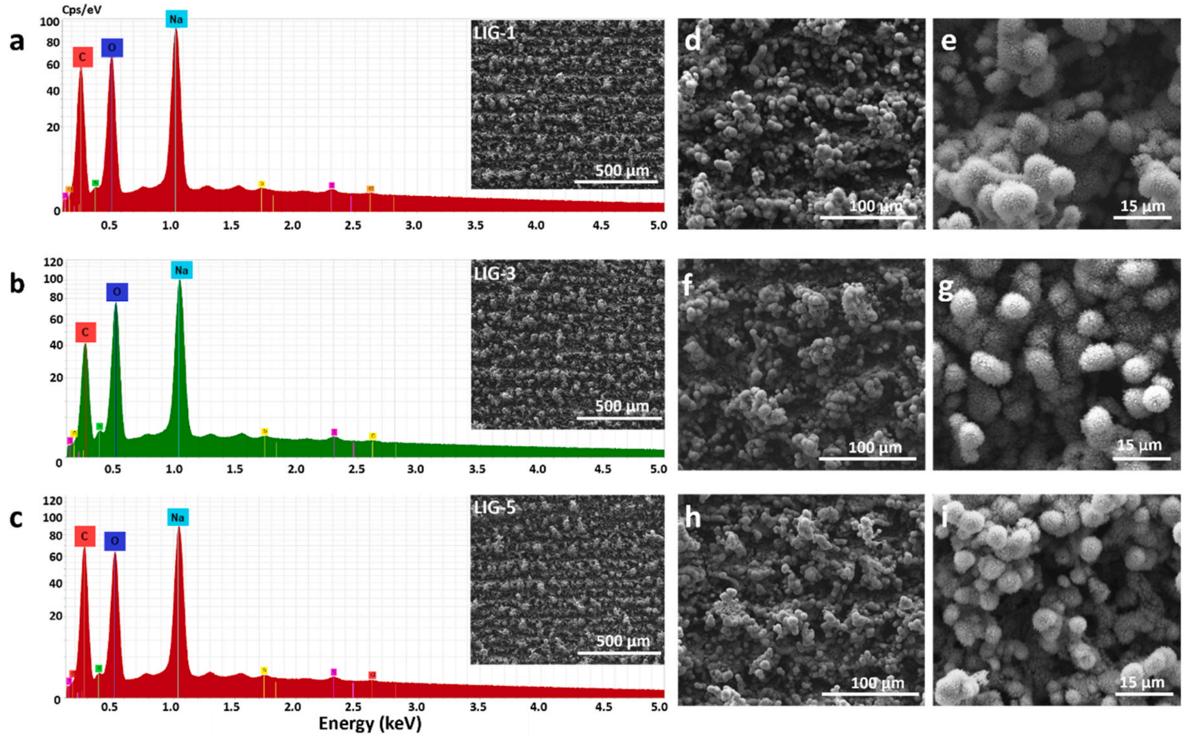

Fig. 2. SEM images and EDS-SEM mapping of LIG. (a–c) EDS-SEM elemental mapping of LIG samples, with corresponding scan areas shown in each figure (scale bar 500 µm). SEM image of LIG-1 (d&e), LIG-3 (f&g), and LIG-5(h&i).

development. Specifically, 48 wt% BDRs in the film were more favorable for the formation of microspheres than 21 and 59 wt% loadings (Fig. S9). The highest S_{BET} value of 375.30 m^2/g was observed with 48 wt% BDR loading (Table S2), which is significantly higher than other biomass-derived LIG (Table S3). Additionally, NaOH as alkali significantly improved uniformity and spheres' size consistency (Fig. S11). Previous studies reported that excessive KOH loading can damage the structural integrity of spherical carbons derived from various biomass-based precursors (e.g., lignin, glucose, sucrose) [39,40]. This phenomenon could be due to the fact that K has superior capability over Na to intercalate into different types of carbon ultrastructure especially at high temperature, disrupting integrity of carbon structure [41]. In short, the proper precursor loading and alkaline agent can effectively promote the microspheres formation in LIG, resulting in optimized specific surface area of BDR-derived LIG for high-performance supercapacitors.

3.2. Supercapacitor performance

SCs can be easily assembled by peeling off the LIG with custom patterns induced on the films (Fig. 3a and b). To investigate the electrochemical performance of SCs fabricated with LIG, systematic exams of CV, GCD, and EIS were performed on the SCs fabricated with LIG-1, -3, and -5 (Fig. 3c). For the SCs developed by LIG-1 that had a thickness of ~50 µm (Fig. S12), all the corresponding CV curves show quasi-rectangular shapes from 0.01 to 0.2 V/s (Fig. 3d), indicating good stability of LIG electrodes under different scan rates. With the applied current densities from 0.2 to 2 mA/cm^2, the GCD curves exhibited fairly triangular shapes, demonstrating its capacitive behaviors (Fig. 3e). The highest C_A of 246 mF/cm^2 was observed when the current density of 0.2 mA/cm^2 was applied. EIS tests were conducted to assess the SC's internal ion transfer resistance. In the high-frequency region of Nyquist plot, the curve intersects the horizontal axis at 51.2 Ω (Fig. 3f). The slope value in the low-frequency region significantly greater than 1 suggests the low impedance of the LIG electrodes (Fig. 3f). The 92.6 % retained capacity of the SC after 10,000 charge-discharge cycles showed its excellent cyclic stability (Fig. 3g). While being bent at different angles (0°, 45°, and 90°), the SCs also showed stable GCD signals across all the bending stages (Fig. S13). In addition, the SCs fabricated with LIG-3 and -5 also demonstrated electrochemical behaviors with remarkable high consistency compared to that based on LIG-1, exhibiting a similar C_A (~240 mF/cm^2) at a current density of 0.2 mA/cm^2 and charge transfer resistances of ~50 Ω (Fig. 3h and S14). It is worthy to note that in all the tests above, we used LIG-3 and -5 induced on the film that was stored for one month under ambient condition after LIG-1 synthesis. Impressively, the quality of the induced LIGs and fabricated SCs remained consistent. Those results showcase the long-term storability and reusability of the films, which are criteria of a precursor for the mass production of LIG-based electronics. Compared to the SCs based on LIG or graphene oxide (GO) derived from other precursors [42–46], the LIG-SCs derived from BDRs exhibited a much higher E_A (27.3 µW h/cm^2) with a P_A of 0.089 mW/cm^2 (Fig. 3i and Table S4). Previous studies showed that doping of N in LIG introduces pseudocapacitance [47,48]. The superior capacitance in the fabricated LIG-SCs can be attributed to the existence of N originating from the precursor [49]. At the high current densities (i.e., 0.8, 1, 2 mA/cm^2), the LIG-SCs primarily exhibited characteristics of double-layer capacitance, evidenced by straight lines in the discharge curves of GCD signals. In contrast, at the lower current densities (i.e., 0.2, 0.5 mA/cm^2), the discharge GCD signals show small curvatures, indicating the occurrence of pseudocapacitance, which can significantly improve the overall capacity of SCs [50]. These findings highlight the tremendous potential of the LIG derived from BDRs for efficient developments of flexible SCs with superior performance.

3.3. Strain sensor performance

Strain sensors can also be facilely assembled by peeling off a LIG pattern from the BDRs film (Fig. 4a). The working principle of a LIG-based strain sensor lies in the formation of microcracks in LIG's internal structure when applied with strain, which decreases the electrical

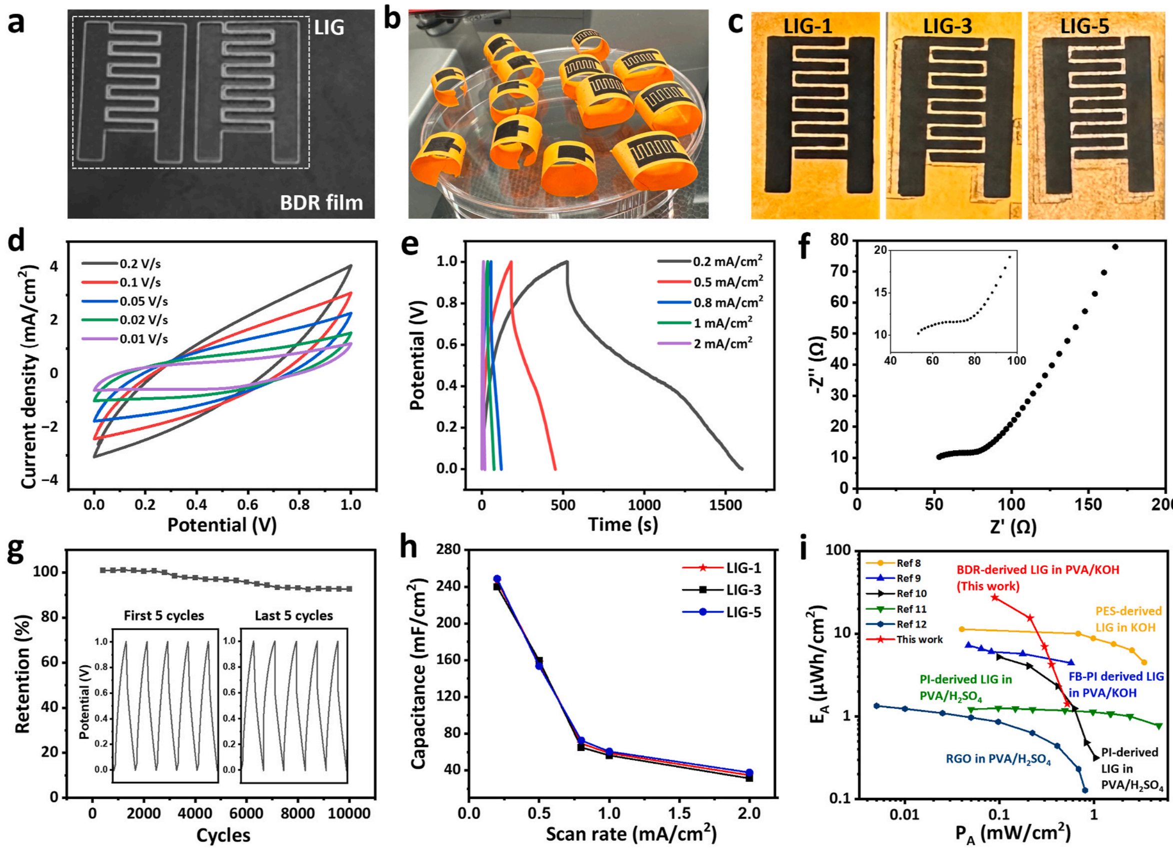

Fig. 3. Electrochemical performance of LIG-SC. (a) LIG induced on the film. (b) Examples of LIG-1 peeled off by tape directly. (c) LIG samples on tape. (d) CV curves at the scan rates from 0.01 to 0.2 V/s with a potential window of 0–1 V. (e) GCD curves at the current density of 0.2–2 mA/cm^2. (f) Nyquist plot. (g) Stability test over 10,000 charge-discharge cycles at the current density of 0.1 mA/cm^2 (h) C_A calculated from the GCD. (i) Area-specific Ragone plot and comparisons with the state-of-art SCs (summarized in Table S4). Polyethersulfone polymer (PES), polyimide (PI), fluorine and boron (FB), reduced graphene oxide (RGO), bio-oil distillation residue (BDR). Ref 8–12 correspond to the citations in Table S4/ Supporting Information.

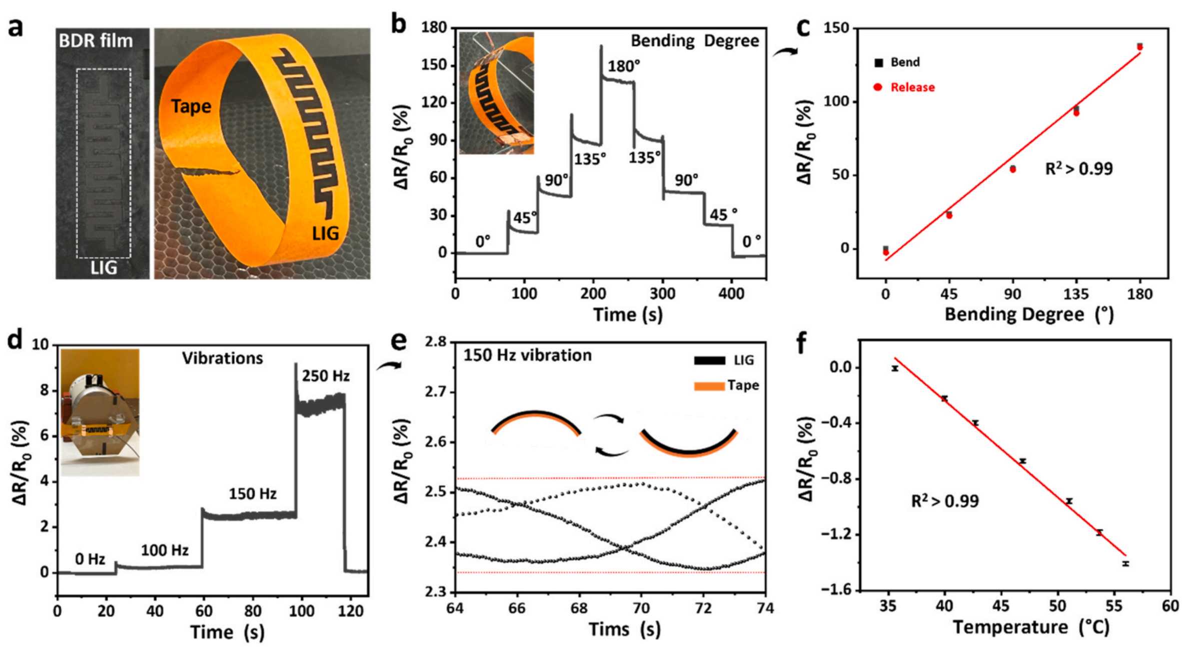

Fig. 4. Performance evaluations on the multifunctional sensor. (a) Pattern of LIG-1 before and after transfer. (b) $\Delta R/R_0$ of the sensor against different bending degrees. (c) Linear fittings on the average values of $\Delta R/R_0$ in each bending state (50 s) in (b). (d) $\Delta R/R_0$ of the sensor against different vibration frequencies (inset: a photo showing how sensor was attached to the shaker). (e) Detailed $\Delta R/R_0$ at a vibration frequency of 150 Hz. (f) Error analysis of $\Delta R/R_0$ of the sensor when exposed to different temperatures.

conductivity between the ends of the LIG pattern. With the excellent mechanical strength of LIG, the altered conductive paths can still be fully reconnected when strain is removed, leading to repeatable resistance changes of the sensor in response to varied strain. Given the limited elasticity of adhesive tape, we focused on the evaluation of the sensor's sensitivity against different bending degrees. Specifically, the sensor was tested when gradually bent from 0 to 180° in 45° increments and then released back to 0° in 45° decrements, held still at each position for 50 s. The signals across all the bending states were stable and repeatable (Fig. 4b). The R^2 values obtained from the linear fitting of signal changes during a complete bending-release cycle were both above 0.99, highlighting the sensor's excellent sensitivity and robustness for practical uses (Fig. 4c). In addition, we examined the sensor's capability in detecting vibrations - fast repeated bending cycles. The sensor was attached to a shaker that provides different vibration frequencies when a LCR meter recorded the sensor's resistance change at a data collection rate of 25 Hz (25 data points in 1 s). The sensor exhibited distinct signal patterns when the frequencies increased from 0 to 100, 150, and 250 Hz (Fig. 4d). This can be attributed to the fact that higher shaking frequencies resulted in a higher degree of deformation of the sensor. Strikingly, the periodic patterns were observed in the rapidly collected signals (Fig. 4e). The highest and lowest values in the signal bands corresponded to the sensor being bent upward and downward, respectively, to the most degrees during the vibration. The bandwidth of the relative resistance change was 0.2 % at 150 Hz and increased to 0.5 % at 250 Hz, compared to the stable horizontal signal line at 0 Hz (Fig. S15). This reflected that 250 Hz vibration resulted in a greater strain than 150 Hz to the sensor, while the sensor was capable to accurately characterize all the vibration states. The well preserved structural integrity of readily detached LIG contributed to the strain's ultrasensitivity [12]. It also resulted in the optimal connections of these conductive pathways in the LIG, which showed significantly enhanced responsiveness of the sensor to deformations caused by external strains.

3.4. Temperature and humidity sensor performance

The sensor was placed horizontally in a temperature-controlled oven with its electrical resistance changes continuously monitored. As the temperature increased from 35 to 56 °C, the overall resistance of the sensor was altered by approximately 1.5 %, with R^2 value of the linear fitting exceeding 0.99 (Fig. 4f). The decrease in LIG conductivity as a function of temperature increase is due to enhanced electron-phonon scattering phenomenon that results in higher electron velocity within its structure [51]. The sensor also showed high sensitivity to humidity from human breath. The working principle is that the adsorption of water molecules into the LIG's structure enhanced its ionic conductivity, leading to resistance changes [52]. Prior studies reported that paper-based LIG humidity sensors with high hysteresis demonstrated response and recovery time of 62 and 126 s, respectively [53–55]. In contrast, superior performance was observed with the sensor fabricated with the BDRs-derived LIG, achieving a rapid signal response in 2 s and speedy returns to its original resistance in 23 s (Fig. S16).

4. Conclusions

This work showed that bio-oil distillation residues (BDRs) can be used as a unique precursor to make a reusable film substrate, yielding highly transferable and stand-alone LIG with consistently high quality. Nanosphere structure and inherent N-doping existed in LIG matrix, which significantly benefited energy storage capacity in supercapacitors (SCs). The SCs showed exceptional energy storage performance with high C_A of 248.7 mF/cm^2, E_A of 27.3 μW h/cm^2 with P_A of 0.089 mW/cm^2, and 92.6 % retention after 10,000 charge-discharge cycles. As a bending sensor, it also exhibited high sensitivity and robustness, accurately detecting subtle deformations caused by vibration as high as 250 Hz with a ~0.2 mm amplitude and specified instantaneous periodic strain changes at a 25 Hz data collecting rate. Furthermore, the sensor demonstrated excellent sensitivity to both temperature (35–56 °C, $R^2 >$ 0.99) and humidity (human breath). These findings indicated that BDRs are a promising precursor for producing consistent high-quality LIG, enabling the induction of self-detached LIG over repeated lasing for effortless transfer. The work would offer a viable strategy toward mass production of LIG in a continuous mode while upgrading BDRs into advanced flexible electronics and wearable devices.

CRediT authorship contribution statement

Shuhong Yang: Writing – original draft, Visualization, Validation, Methodology, Investigation, Formal analysis, Data curation, Conceptualization. **Yaseen Elkasabi:** Writing – review & editing, Resources. **Qiangu Yan:** Formal analysis, Resources, Validation, Writing – review & editing. **Bujingda Zheng:** Writing – review & editing, Software. **Honghua Qian:** Writing – review & editing, Resources. **Jian Lin:** Writing – review & editing, Resources. **Caixia Wan:** Writing – review & editing, Validation, Supervision, Resources, Project administration, Methodology, Investigation, Funding acquisition.

Notes

The authors declare that they have no competing interests.

Experiments on human subjects

The evaluations of sensor and SCs were conducted under the approval from the University of Missouri-Columbia Institutional Review Board (Project Number: 2093707). All human subjects gave written, informed consent before participation in the study.

Declaration of competing interest

The authors declare that they have no known competing financial interests or personal relationships that could have appeared to influence the work reported in this paper.

Acknowledgements

This work was supported by the National Science Foundation (Award No. 1933861) and the USDA Forest Service (Grant No. 23-JV-11111124-053).

Appendix A. Supplementary data

Supplementary data to this article can be found online at https://doi.org/10.1016/j.carbon.2025.120301.

References

[1] A.C. Bressi, A. Dallinger, Y. Steksova, F. Greco, Bioderived laser-induced graphene for sensors and supercapacitors, ACS Appl. Mater. Interfaces 15 (30) (2023) 35788–35814.
[2] J.S. Jayan, S.S. Jayan, Biomass-derived laser-induced graphene and its advances in the electronic applications, Adv. Eng. Mater. 25 (16) (2023) 2300248.
[3] O. Yu, K.H. Kim, Lignin to materials: a focused review on recent novel lignin applications, Appl. Sci. (Basel). 10 (13) (2020) 4626.
[4] A. Nag, R.B.V.B. Simorangkir, D.R. Gawade, S. Nuthalapati, J.L. Buckley, B. O'Flynn, M.E. Altinsoy, S.C. Mukhopadhyay, Graphene-based wearable temperature sensors: a review, Mater. Des. 221 (2022) 110971.
[5] W.J. Yu, W.W. Zhao, S.P. Wang, Q. Chen, X.Q. Liu, Direct conversion of liquid organic precursor into 3d laser-induced graphene materials, Adv. Mater. 35 (9) (2023) 2209545.
[6] M. Mu, G.M. Chen, W.J. Yu, J.M. Liu, Y.J. Wang, W.W. Zhao, X.Q. Liu, In situ growth of laser-induced graphene on flexible substrates for wearable sensors, ACS Appl. Nano Mater. 7 (3) (2024) 3279–3288.
[7] H. Wang, Z.F. Zhao, P.P. Liu, X.G. Guo, Laser-induced graphene based flexible electronic devices, Biosens.-Basel 12 (2) (2022) 55.

[8] T.R. Cui, D. Li, T. Hirtz, W.C. Shao, Z.B. Zhou, S.R. Ji, X. Li, J.D. Xu, J.M. Jian, Z. K. Chen, et al., Laser-induced graphene for multifunctional and intelligent wearable systems: for health care and human-computer interaction, Appl. Sci.-Basel 13 (8) (2023) 4688.
[9] R.Q. Ye, Y. Chyan, J.B. Zhang, Y.L. Li, X. Han, C. Kittrell, J.M. Tour, Laser-induced graphene formation on wood, Adv. Mater. 29 (37) (2017) 1702211.
[10] C.H. Dreimol, H.Z. Guo, M. Ritter, T. Keplinger, Y. Ding, R. Günther, E. Poloni, I. Burgert, G. Panzarasa, Sustainable wood electronics by iron-catalyzed laser-induced graphitization for large-scale applications, Nat. Commun. 13 (1) (2022) 3680.
[11] T.S.D. Le, S. Park, J.N. An, P.S. Lee, Y.J. Kim, Ultrafast laser pulses enable one-step graphene patterning on woods and leaves for green electronics, Adv. Funct. Mater. 29 (33) (2019) 1902771.
[12] S.H. Yang, Y. Ling, Q. Wu, H.W. Zhang, Z. Yan, G.L. Huang, J. Lin, C.X. Wan, Lignin-derived porous graphene for wearable and ultrasensitive strain sensors, J. Mater. Chem. C Mater 10 (32) (2022) 11730–11738.
[13] R. Rahimi, M. Ochoa, A. Tarnayol, S. Khalili, A. Khademhosseini, B. Ziaie, Highly stretchable potentiometric Ph sensor fabricated via laser carbonization and machining of carbon-polyaniline composite, ACS Appl. Mater. Interfaces 9 (10) (2017) 9015–9023.
[14] C.P. Sharma, C.J. Arnusch, Laser-induced graphene composite adhesive tape with electro-photo-thermal heating and antimicrobial capabilities, Carbon 196 (2022) 102–109.
[15] A. Dallinger, K. Keller, H. Fitzek, F. Greco, Stretchable and skin-conformable conductors based on Polyurethane/laser-induced graphene, ACS Appl. Mater. Interfaces 12 (17) (2020) 19855–19865.
[16] Q.S. Li, T.Y. Wu, W. Zhao, J.W. Ji, G. Wang, Laser-induced corrugated graphene films for integrated multimodal sensors, ACS Appl. Mater. Interfaces 13 (31) (2021) 37423–37434.
[17] T. Pinheiro, R. Correia, M. Morais, J. Coelho, E. Fortunato, M.G.F. Sales, A. C. Marques, R. Martins, Water peel-off transfer of electronically enhanced, paper-based laser-induced graphene for wearable electronics, ACS Nano 16 (12) (2022) 20633–20646.
[18] A. Kaidarova, J. Kosel, Physical sensors based on laser-induced graphene: a review, IEEE Sens. J. 21 (11) (2021) 12426–12443.
[19] X.S. Zhang, G.X. Yang, H. Jiang, W.J. Liu, H.S. Ding, Mass production of chemicals from biomass-derived oil by directly atmospheric distillation coupled with Co-Pyrolysis, Sci. Rep. 3 (2013) 1120.
[20] Y. Elkasabi, C.A. Mullen, M.A. Jackson, A.A. Boateng, Characterization of fast-pyrolysis bio-oil distillation residues and their potential applications, Anal. Appl. Pyrolysis. 114 (2015) 179–186.
[21] S. Movaghgharnezhad, P.L.Y. Kang, Laser-induced graphene: synthesis advances, structural tailoring, enhanced properties, and sensing applications, J. Mater. Chem. C Mater 12 (19) (2024) 6718–6742.
[22] J. Lin, Z.W. Peng, Y.Y. Liu, F. Ruiz-Zepeda, R.Q. Ye, E.L.G. Samuel, M.J. Yacaman, B.I. Yakobson, J.M. Tour, Laser-induced porous graphene films from commercial polymers, Nat. Commun. 5 (2014) 5714.
[23] P.I.C. Claro, T. Pinheiro, S.L. Silvestre, A.C. Marques, J. Coelho, J.M. Marconcini, E. Fortunato, L.H.C. Mattoso, R. Martins, Sustainable carbon sources for green laser-induced graphene: a perspective on fundamental principles, applications, and challenges, Appl. Phys. Rev. 9 (4) (2022) 041305.
[24] J.B. Zhu, X. Huang, W.X. Song, Physical and chemical sensors on the basis of laser-induced graphene: mechanisms, applications, and perspectives, ACS Nano 15 (12) (2021) 18708–18741.
[25] H.R. Moon, B. Ryu, Review of laser-induced graphene (lig) produced on eco-friendly substrates, Int J Pr Eng Man-Gt 11 (4) (2024) 1279–1294.
[26] Y. Lin, L.B. Freund, Forced detachment of a vesicle in adhesive contact with a substrate, Int. J. Solid Struct. 44 (6) (2007) 1927–1938.
[27] B. Orbán, T. Höltzl, The promoter role of sulfur in carbon nanotube growth, Dalton Trans. 51 (24) (2022) 9256–9264.
[28] R. Alexander, A. Dinkar, S. Biswas, K. Dasgupta, Comparative study of different carbon reinforcements at different length scales on the properties of polyvinyl alcohol composites, Polym. Compos. 42 (9) (2021) 4239–4252.
[29] D.F. Li, J. Li, P.C. Wu, G.Y. Zhao, Q.A. Qu, X.E. Yu, Recent advances in electrically driven soft actuators across dimensional scales from 2d to 3d, Adv. Intell. Syst.-Ger. 6 (2) (2024) 2300070.
[30] W.J. Yu, Y.Y. Peng, L.J. Cao, W.W. Zhao, X.Q. Liu, Free-standing laser-induced graphene films for high-performance electromagnetic interference shielding, Carbon 183 (2021) 600–611.
[31] S. Roscher, R. Hoffmann, O. Ambacher, Determination of the graphene-graphite ratio of graphene powder by raman 2d band symmetry analysis, Anal. Methods 11 (9) (2019) 1224–1228.
[32] O.V. Kharissova, B.I. Kharisov, Variations of interlayer spacing in carbon nanotubes, RSC Adv. 4 (58) (2014) 30807–30815.
[33] Y.A. Wang, Y. Wang, P.P. Zhang, F. Liu, S.D. Luo, Laser-induced freestanding graphene papers: a new route of scalable fabrication with tunable morphologies and properties for multifunctional devices and structures, Small 14 (36) (2018) 1802350.
[34] H.B. Liu, H.E. Jiang, F. Du, D.P. Zhang, Z.J. Li, H.W. Zhou, Flexible and degradable paper-based strain sensor with low cost, ACS Sustain. Chem. Eng. 5 (11) (2017) 10538–10543.
[35] N. Dixit, S.P. Singh, Laser-induced graphene (lig) as a smart and sustainable material to restrain pandemics and endemics: a perspective, ACS Omega 7 (6) (2022) 5112–5130.
[36] G.J. Li, Direct laser writing of graphene electrodes, J. Appl. Phys. 127 (1) (2020) 010901.
[37] X.T. Chen, Y. Wu, W.H. Gu, M. Zhou, S.L. Tang, J.M. Cao, Z.Q. Zou, G.B. Ji, Research progress on nanostructure design and composition regulation of carbon spheres for the microwave absorption, Carbon 189 (2022) 617–633.
[38] Y. Fang, L. Liu, H. Xiang, Y. Wang, X. Sun, Biomass-based carbon microspheres for removing heavy metals from the environment: a review, Mater. Today Sustain. 18 (2022) 100136.
[39] A.J. Romero-Anaya, M. Ouzzine, M.A. Lillo-Ródenas, A. Linares-Solano, Spherical carbons: synthesis, characterization and activation processes, Carbon 68 (2014) 296–307.
[40] K.L.A. Cao, Y. Kitamoto, F. Iskandar, T. Ogi, Sustainable porous hollow carbon spheres with high specific surface area derived from kraft lignin, Adv. Powder Technol. 32 (6) (2021) 2064–2073.
[41] E. Raymundo-Piñero, P. Azaïs, T. Cacciaguerra, D. Cazorla-Amorós, A. Linares-Solano, F. Béguin, Koh and naoh activation mechanisms of multiwalled carbon nanotubes with different structural organisation, Carbon 43 (4) (2005) 786–795.
[42] M.R.R. Abdul-Aziz, A. Hassan, A.A.R. Abdel-Aty, M.R. Saber, R. Ghannam, B. Anis, H. Heidari, A.S.G. Khalil, High performance supercapacitor based on laser induced graphene for wearable devices, IEEE Access 8 (2020) 200573–200580.
[43] H. Awasthi, H. Renuka, A.K. Srivastava, S. Goel, Laser-induced graphene-based flexible interdigital electrode realizing micro supercapacitor sustainable in different temperatures, ESS. 5 (3) (2023) e405.
[44] Z. Peng, J. Lin, R. Ye, E.L.G. Samuel, J.M. Tour, Flexible and stackable laser-induced graphene supercapacitors, ACS Appl. Mater. Interfaces 7 (5) (2015) 3414–3419.
[45] Y. Wu, Y.X. Zhang, Y.P. Liu, P. Cui, S.B. Chen, Z.X. Zhang, J.C. Fu, E.Q. Xie, Boosting the electrochemical performance of graphene-based on-Chip micro-supercapacitors by regulating the functional groups, ACS Appl. Mater. Interfaces 12 (38) (2020) 42933–42941.
[46] G.Y. Yuan, T. Wan, A. BaQais, Y.R. Mu, D.P. Cui, M.A. Amin, X.D. Li, B.B. Xu, X. H. Zhu, H. Algadi, et al., Boron and fluorine Co-Doped laser-induced graphene towards high-performance micro-supercapacitors, Carbon 212 (2023) 118101.
[47] K. Rhili, S. Chergui, J.C. Abergo-Martinez, A.S. El Douhaibi, M. Siaj, Phosphorus and nitrogen Co-Doped reduced graphene oxide as superior electrode nanomaterials for supercapacitors, Mater. Adv. 4 (21) (2023) 5263–5272.
[48] J.C. Fan, Y.J. Zheng, Z.S. Zhao, W.Y. Guo, S. Zhu, Nitrogen, phosphorus, and sulfur tri-doped carbon a coated nicose needle arrays grown on carbon cloth as binder-free anode for potassium-ion batteries, Fmats 9 (2022) 875684.
[49] M. Reina, A. Scalia, G. Auxilia, M. Fontana, F. Bella, S. Ferrero, A. Lamberti, Boosting electric double layer capacitance in laser-induced graphene-based supercapacitors, Adv. Sustain. Syst. 6 (1) (2022) 2100228.
[50] S. Fleischmann, J.B. Mitchell, R.C. Wang, C. Zhan, D.E. Jiang, V. Presser, V. Augustyn, Pseudocapacitance: from fundamental understanding to high power energy storage materials, Chem. Rev. 120 (14) (2020) 6738–6782.
[51] Q. Shao, G. Liu, D. Teweldebrhan, A.A. Balandin, High-temperature quenching of electrical resistance in graphene interconnects, Appl. Phys. 92 (20) (2008) 202108.
[52] R.X. Liang, A.S. Luo, Z.B. Zhang, Z.T. Li, C.Y. Han, W.B. Wu, Research progress of graphene-based flexible humidity sensor, Sensors 20 (19) (2020) 5601.
[53] M. Mraovic, T. Muck, M. Pivar, J. Trontelj, A. Pletersek, Humidity sensors printed on recycled paper and cardboard, Sensors 14 (8) (2014) 13628–13643.
[54] G. Niarchos, G. Dubourg, G. Afroudakis, M. Georgopoulos, V. Tsouti, E. Makarona, V. Crnojevic-Bengin, C. Tsamis, Humidity sensing properties of paper substrates and their passivation with Zno nanoparticles for sensor applications, Sensors 17 (3) (2017) 516.
[55] R. Rahimi, M. Ochoa, B. Ziaie, Comparison of direct and indirect laser ablation of metallized paper for inexpensive paper-based sensors, ACS Appl. Mater. Interfaces 10 (42) (2018) 36332–36341.